J. Fluid Mech. (1988), *vol.* 187, *pp.* 329–352
Printed in Great Britain

Three-dimensional Rayleigh–Taylor instability Part 1. Weakly nonlinear theory

By J. W. JACOBS† AND I. CATTON
Department of Mechanical, Aerospace and Nuclear Engineering, University of California, Los Angeles, CA 90024, USA

(Received 24 February 1987 and in revised form 29 July 1987)

Three-dimensional weakly nonlinear Rayleigh–Taylor instability is analysed. The stability of a confined inviscid liquid and an overlying gas with density much less than that of the liquid is considered. An asymptotic solution for containers of arbitrary cross-sectional geometry, valid up to order ϵ^3 (where ϵ is the root-mean-squared initial surface slope) is obtained. The solution is evaluated for the rectangular and circular geometries and for various initial modes (square, hexagonal, axisymmetric, etc.). It is found that the hexagonal and axisymmetric instabilities grow faster than any other shapes in their respective geometries. In addition it is found that, sufficiently below the cutoff wavenumber, instabilities that are equally proportioned in the lateral directions grow faster than those with longer, thinner shape. However, near the cutoff wavenumber this trend reverses with instabilities having zero aspect ratio growing faster than those with aspect ratio near 1.

1. Introduction

One of the most fundamental hydrodynamic instabilities occurs when an interface separating two fluids is accelerated into the heavier fluid. The existence of the instability is universally understood; everyone intuitively knows that when a container of water is turned upside down the water falls out. However, the study of this seemingly simple phenomenon has challenged researchers for over four decades. Early interest in the subject was motivated by applications to nuclear weapons. More recently, Rayleigh–Taylor instability has found a wider spectrum of interest in such fields as geophysics and astrophysics as well as nuclear safety. Taylor (1950) considered the linear stability of an unstably stratified two-fluid system and obtained an expression governing the growth of the unstable surface waves. Later Bellman & Pennington (1954) added surface tension and viscosity to Taylor's linear theory. Early on it was recognized that the inherent nonlinearity of the problem played an important role in the growth of the instability as soon as the surface waves grew to an appreciable height. Emmons, Chang & Watson (1960) addressed this problem by performing a weakly nonlinear asymptotic analysis of the two-dimensional instability. Later Nayfeh (1969) corrected an error in their analysis where they failed to account for the singular nature of the perturbation problem.

Though weakly nonlinear theory provides useful information concerning the effects of nonlinearity on the instability, it was recognized that, like the linear theory, the weakly nonlinear theory was valid only for instabilities of small amplitude. Other researchers (Fermi & Von Neumann 1960; Layzer 1955; Dienes 1978; Baker & Freeman 1981) have used simplified models to study the nonlinear

† Present address: California Institute of Technology, Pasadena, CA 91125, USA.

instability. This work suffers from the fact that the accuracy of these models can only be determined empirically. On the other hand, numerical methods (Harlow & Welch 1966; Daly 1967, 1969; Baker, Meiron & Orzag 1980; Pullin 1982; Menikoff & Zemach 1983) have yielded reliable results; however, numerical calculations of Rayleigh–Taylor instability with large surface displacement remains a formidable problem, even by today's standards, requiring a significant amount of computational resources.

Because of the difficulty in analysing the nonlinear instability, essentially all of the work done to date has been concentrated on the two-dimensional geometry. It is the aim of this work to analyse the three-dimensional instability. Weakly nonlinear theory, while being significantly less difficult than a numerical method, has proven to yield dependable results within its region of validity. We develop a weakly nonlinear three-dimensional asymptotic solution of Rayleigh–Taylor instability in enclosures of arbitrary cross-sectional geometry. We then evaluate this solution for several instabilities in both rectangular and circular geometries. To simplify the analysis we consider the instability of two inviscid, incompressible fluids with a large difference in density. The method of analysis follows that of Nayfeh (1969) with extensive use of the notation of Miles (1976).

2. Mathematical formulation

We consider the irrotational motion of an inviscid liquid of density ρ contained in a cylindrical basin Ω with cross section S' and unit outward normal $\boldsymbol{n}$. Let d' be the undisturbed depth of the liquid and $\boldsymbol{x}'$ and z' be the horizontal and vertical coordinates in a reference frame fixed in Ω so that $z' = \eta'(\boldsymbol{x}', t')$ and $z' = -d$ at the bottom. Let $\phi'(\boldsymbol{x}', z', t')$ be the velocity potential (defined as $\nabla\phi$ = the fluid velocity relative to Ω) and g be the acceleration of Ω relative to a free-falling reference frame and perpendicular to the quiescent interface (positive when in the positive z' direction). We assume the overlying fluid to be a gas with density much less than the density of the liquid so that its effect on the motion of the liquid can be neglected; however we include surface tension γ.

For the purpose of making the governing equations dimensionless we choose as a length scale $1/k'$, where k' is the wavenumber of the initial disturbance, and as a velocity scale $(g/k')^{\frac{1}{2}}$. We then define the following dimensionless variables:

$$\boldsymbol{x} = k'\boldsymbol{x}', \quad z = k'z', \quad t = t'(gk')^{\frac{1}{2}}, \quad \eta = k'\eta', \quad \phi = \phi'(k'^3/g)^{\frac{1}{2}}. \tag{2.1}$$

In terms of these variables, the governing equations and boundary conditions are

$$\nabla^2\phi = 0 \quad (\boldsymbol{x} \text{ in } S,\ -d < z < \eta), \tag{2.2a}$$

$$\eta_t + \nabla\phi\cdot\nabla\eta - \phi_z = 0 \quad (\boldsymbol{x} \text{ in } S,\ z = \eta), \tag{2.2b}$$

$$\phi_t + \tfrac{1}{2}(\nabla\phi)^2 - \eta - K^2\nabla\cdot\left\{\frac{\nabla\eta}{[1+(\nabla\eta)^2]^{\frac{1}{2}}}\right\} = 0 \quad (\boldsymbol{x} \text{ in } S,\ z = \eta), \tag{2.2c}$$

$$\nabla\phi\cdot\boldsymbol{n} = 0 \quad (\text{on } \Omega), \tag{2.2d}$$

where $d = k'd'$, $S = k'^2S'$. The parameter K is given by

$$K = \frac{k'}{k'_c}, \tag{2.3}$$

and k_c', the cutoff wavenumber, is given by

$$k_c' = \left(\frac{\rho g}{\gamma}\right)^{\frac{1}{2}}. \tag{2.4}$$

For small amplitude, ϕ can be expanded in a Taylor series about the undisturbed interfacial position ($\eta = 0$). This allows (2.2*b*) and (2.2*c*) to be applied at $\eta = 0$, yielding the following conditions:

$$\left.\begin{aligned} &\eta_t + \nabla\phi\cdot\nabla\eta + \eta\nabla\phi_z\cdot\nabla\eta - \phi_z - \eta\phi_{zz} - \tfrac{1}{2}\eta^2\phi_{zzz} + \ldots = 0 \qquad (2.5a)\\ &\phi_t + \eta\phi_{tz} + \tfrac{1}{2}\eta^2\phi_{tzz} + \tfrac{1}{2}(\nabla\phi)^2 + \eta\nabla\phi\cdot\nabla\phi_z - \eta \\ &\qquad - K^2\nabla^2\eta + \tfrac{1}{2}K^2\nabla\cdot[\nabla\eta(\nabla\eta)^2] + \ldots = 0 \qquad (2.5b)\end{aligned}\right\} \quad (\boldsymbol{x} \text{ in } S,\ z = 0).$$

If the amplitude of the instability is sufficiently small, we expect the nonlinear solution to be reasonably close to the solution of the linear problem. With this in mind we expand η and ϕ in what can be considered to be time-dependent Fourier series

$$\eta(\boldsymbol{x}, t) = \sum_n a_n(t)\,\psi_n(\boldsymbol{x}), \tag{2.6a}$$

$$\phi(\boldsymbol{x}, z, t) = \sum_n b_n(t)\,\chi_n(\boldsymbol{x}, z), \tag{2.6b}$$

where ψ_n and χ_n are eigenfunctions of the linear problem, determined from satisfying (2.2*a*) and (2.2*d*). More explicitly, ψ_n and χ_n are related by

$$\chi_n(\boldsymbol{x}, z) = \psi_n(\boldsymbol{x})\,\frac{\cosh k_n(z+d)}{\cosh k_n d}, \tag{2.7a}$$

where ψ_n satisfy

$$(\nabla^2 + k_n^2)\,\psi_n = 0, \tag{2.7b}$$

$$\nabla\psi_n\cdot\boldsymbol{n} = 0 \quad (\text{on } \partial S), \tag{2.7c}$$

with

$$k_n = |\boldsymbol{k}_n| \tag{2.7d}$$

and

$$\iint \psi_m\psi_n\,\mathrm{d}S = \delta_{mn}S \quad \left(\delta_{mn} = \begin{matrix}1, & m = n\\ 0, & m \neq n\end{matrix}\right) \tag{2.7e}$$

specifies ψ_n to be orthonormal.

Substituting (2.6) into (2.5), then weighting with ψ_n and integrating $\iint\cdot\,\mathrm{d}S$ yields the following system of ordinary differential equations:

$$\dot{a}_j - \kappa_j b_j = \sum_{l,m}[a_l b_m k_m^2 C_{jlm} - a_l b_m D_{jlm}] + \sum_{l,m,n}[\tfrac{1}{2}a_l a_m b_n \kappa_n k_n^2 C_{jlmn} - a_l a_m b_n \kappa_n D_{jlmn}] + \text{H.O.T.}, \tag{2.8a}$$

$$\dot{b}_j - (1 - k_j^2 K^2)\,a_j = \sum_{l,m}[-a_l \dot{b}_m \kappa_m C_{jlm} - \tfrac{1}{2}b_l b_m (D_{jlm} + \kappa_l\kappa_m C_{jlm})] + \sum_{l,m,n}[-\tfrac{1}{2}a_l a_m \dot{b}_n k_n^2 C_{jlmn} - a_l b_m b_n (\kappa_n D_{jlmn} + \kappa_m k_n^2 C_{jlmn}) + \tfrac{1}{2}K^2 a_l a_m a_n E_{jlmn}] + \text{H.O.T.}, \tag{2.8b}$$

where

$$C_{lmn} = \frac{1}{S}\int\int \psi_l \psi_m \psi_n \, \mathrm{d}S, \tag{2.9a}$$

$$C_{jlmn} = \frac{1}{S}\int\int \psi_j \psi_l \psi_m \psi_n \, \mathrm{d}S, \tag{2.9b}$$

$$D_{lmn} = \frac{1}{S}\int\int \psi_l (\nabla\psi_m \cdot \nabla\psi_n) \, \mathrm{d}S, \tag{2.9c}$$

$$D_{jlmn} = \frac{1}{S}\int\int \psi_j \psi_l (\nabla\psi_m \cdot \nabla\psi_n) \, \mathrm{d}S, \tag{2.9d}$$

$$E_{jlmn} = \frac{1}{S}\int\int (\nabla\psi_j \cdot \nabla\psi_l)(\nabla\psi_m \cdot \nabla\psi_n) \, \mathrm{d}S \tag{2.9e}$$

and

$$\kappa_n = k_n \tanh(k_n d). \tag{2.10}$$

The following formulae are obtained using integration by parts:

$$D_{lmn} = \tfrac{1}{2} C_{lmn}(k_m^2 + k_n^2 - k_l^2), \tag{2.11a}$$

$$D_{jlmn} = k_m^2 C_{jlmn} - D_{njlm} - D_{nljm}. \tag{2.11b}$$

Repeated application of (2.11*b*) gives

$$D_{mnnn} = (\tfrac{1}{2}k_n^2 - \tfrac{1}{6}k_m^2) C_{mnnn} \tag{2.11c}$$

and

$$D_{nnnn} = \tfrac{1}{3} k_n^2 C_{nnnn}. \tag{2.11d}$$

3. The outer solution

We seek a solution to (2.8) satisfying the following initial conditions:

$$a_1(0) = \epsilon, \quad b_1(0) = 0, \quad a_n(0) = b_n(0) = 0 \quad (n \neq 1), \tag{3.1a, b, c}$$

where $\epsilon \ll 1$. Physically, these conditions correspond to an initial surface deflection consisting of a single Fourier mode with r.m.s. slope ϵ, and zero initial velocity. We then implement the 'method of strained coordinates' (Van Dyke 1975). Expanding in terms of the small parameter ϵ we obtain

$$a_n = \epsilon\delta_{n1} a_{11}(\tau) + \epsilon^2 a_{2n}(\tau) + \epsilon^3 a_{3n}(\tau) + \ldots, \tag{3.2a}$$

$$b_n = \epsilon\delta_{n1} b_{11}(\tau) + \epsilon^2 b_{2n}(\tau) + \epsilon^3 b_{3n}(\tau) + \ldots, \tag{3.2b}$$

$$\tau = t(1 + \epsilon^2\mu_2 + \ldots), \tag{3.2c}$$

where $k_1 = 1$ and $\kappa_1 = T = \tanh d$. Substituting these expansions into (2.8) and equating like powers of ϵ we obtain at order-ϵ a system of o.d.e.'s governing the growth of the linear instability

$$\dot{a}_{11} - T b_{11} = 0, \quad \dot{b}_{11} - (1 - K^2) a_{11} = 0. \tag{3.3a, b}$$

The solution of this system is

$$a_{11} = \cosh \sigma_1 \tau, \quad b_{11} = \frac{\sigma_1}{T} \sinh \sigma_1 \tau, \tag{3.4a, b}$$

where

$$\sigma_1^2 = T(1 - K^2). \tag{3.5}$$

Note that geometry does not enter in the linear solution. We must go to higher order to find the influence of geometry.

At order-ϵ^2 we obtain a system of o.d.e.'s with the same left-hand side as the first-order equations and forced by quadratic combinations of the first-order solution

$$\dot{a}_{2n} - \kappa_n b_{2n} = a_{11} b_{11} (C_{n11} - D_{n11}), \tag{3.6a}$$

$$\dot{b}_{2n} - (1 - k_n^2 K^2) a_{2n} = -a_{11} \dot{b}_{11} T C_{n11} - \tfrac{1}{2} b_{11}^2 (D_{n11} + T^2 C_{n11}). \tag{3.6b}$$

This system has the following solution:

$$a_{2n} = A_{2n}^{(1)} (\cosh 2\sigma_1 \tau - \cosh \sigma_n \tau) + A_{2n}^{(2)} (1 - \cosh \sigma_n \tau), \tag{3.7a}$$

$$b_{2n} = B_{2n}^{(1)} \sinh 2\sigma_1 \tau + B_{2n}^{(2)} \sinh \sigma_n \tau, \tag{3.7b}$$

where

$$\sigma_n^2 = \kappa_n (1 - k_n^2 K^2) \tag{3.8}$$

and

$$A_{2n}^{(1)} = \frac{\sigma_1^2 [4T k_n^2 - \kappa_n (6T^2 + 2 - k_n^2)]}{8T^2 (4\sigma_1^2 - \sigma_n^2)} C_{n11}, \tag{3.9a}$$

$$A_{2n}^{(2)} = \frac{\sigma_1^2 \kappa_n (2T^2 - 2 + k_n^2)}{8T^2 \sigma_n^2} C_{n11}, \tag{3.9b}$$

$$B_{2n}^{(1)} = \frac{2\sigma_1 A_{2n}^{(1)}}{\kappa_n} - \frac{\sigma_1 k_n^2}{4T\kappa_n} C_{n11}, \tag{3.9c}$$

$$B_{2n}^{(2)} = -\frac{\sigma_n (A_{2n}^{(1)} + A_{2n}^{(2)})}{\kappa_n}. \tag{3.9d}$$

Finally, at order-ϵ^3 we obtain a system this time forced by combinations of both the first- and second-order solutions

$$\begin{aligned} \dot{a}_{3m} - \kappa_m b_{3m} = \sum_n [a_{11} b_{2n} (k_n^2 C_{m1n} - D_{m1n}) + a_{2n} b_{11} (C_{mn1} - D_{mn1})] \\ + a_{11}^2 b_{11} T (\tfrac{1}{2} C_{m111} - D_{m111}) - \dot{a}_{11} \mu_2 \delta_{m1}, \end{aligned} \tag{3.10a}$$

$$\begin{aligned} \dot{b}_{3m} - (1 - k_m^2 K^2) a_{3m} = \sum_n [-b_{11} b_{2n} (D_{m1n} + T\kappa_n C_{m1n}) - a_{2n} \dot{b}_{11} T C_{mn1} \\ - a_{11} \dot{b}_{2n} \kappa_n C_{m1n}] - \tfrac{1}{2} a_{11}^2 \dot{b}_{11} C_{m111} - a_{11} b_{11}^2 T (D_{m111} + C_{m111}) \\ + \tfrac{1}{2} K^2 a_{11}^3 E_{m111} - \dot{b}_{11} \mu_2 \delta_{m1}. \end{aligned} \tag{3.10b}$$

After substituting for the lower-order solutions we obtain

$$\begin{aligned} \dot{a}_{3m} - \kappa_m b_{3m} = P_m^{(1)} \sinh \sigma_1 \tau + P_m^{(2)} \sinh 3\sigma_1 \tau \\ + \sum_n [P_{mn}^{(3)} \sinh (\sigma_1 - \sigma_n) \tau + P_{mn}^{(4)} \sinh (\sigma_1 + \sigma_n) \tau] - \sigma_1 \mu_2 \delta_{m1} \sinh \sigma_1 \tau, \end{aligned} \tag{3.11a}$$

$$\begin{aligned} \dot{b}_{3m} - (1 - K^2 k_m^2) a_{3m} = Q_m^{(1)} \cosh \sigma_1 \tau + Q_m^{(2)} \cosh 3\sigma_1 \tau \\ + \sum_n [Q_{mn}^{(3)} \cosh (\sigma_1 - \sigma_n) \tau + Q_{mn}^{(4)} \cosh (\sigma_1 + \sigma_n) \tau] - \frac{\sigma_1^2}{T} \mu_2 \delta_{m1} \cosh \sigma_1 \tau, \end{aligned} \tag{3.11b}$$

where $P_m^{(1)}$, $P_m^{(2)}$, $P_{mn}^{(3)}$, $P_{mn}^{(4)}$ and $Q_m^{(1)}$, $Q_m^{(2)}$, $Q_{mn}^{(3)}$, $Q_{mn}^{(4)}$ are constants (given in Appendix A). Eliminating b_{3m} we obtain

$$\begin{aligned}\ddot{a}_{3m}-\kappa_m(1-K^2k_m^2)\,a_{3m} = {} & [\sigma_1 P_m^{(1)}+\kappa_m Q_m^{(1)}-2\sigma_1^2\mu_2\delta_{m1}]\cosh\sigma_1\tau \\ & +[3\sigma_1 P_m^{(2)}+\kappa_m Q_m^{(2)}]\cosh 3\sigma_1\tau \\ & +\sum_n[(\sigma_1-\sigma_n)P_{mn}^{(3)}+\kappa_m Q_{mn}^{(3)}]\cosh(\sigma_1-\sigma_n)\tau \\ & +\sum_n[(\sigma_1+\sigma_n)P_{mn}^{(4)}+\kappa_m Q_{mn}^{(4)}]\cosh(\sigma_1+\sigma_n)\tau. \quad (3.12)\end{aligned}$$

Ordinarily, a secular term (i.e. a term of the type $t\cosh\sigma_1 t$) would appear in the solution of (3.12) with $m=1$. When $K>1$, σ_1 is imaginary and the secularity will eventually cause a_{31} to overtake a_{21} and a_{11}, and thus cause the asymptotic series to become disordered. Applying the method of strained coordinates allows the secular term to be suppressed by the proper choice of the constant μ_2. However, when $K<1$, σ_1 is real and the rapid growth of all the terms in a_{31} causes the asymptotic series to become disordered long before the secularity becomes important. Thus, elimination of the secular term when $K<1$ is of questionable utility. Either way, suppressing the secularity does not make the solution any less valid; therefore, in order to obtain the best solution for all values of K, we shall apply the method of strained coordinates. The coefficient multiplying $\cosh\sigma_1\tau$ in (3.12) when $m=1$ must be set to zero. This is accomplished by choosing

$$\mu_2=\frac{\sigma_1 P_1^{(1)}+\kappa_1 Q_1^{(1)}}{2\sigma_1^2}. \quad (3.13)$$

The solution of the third-order problem is then

$$\begin{aligned}a_{3m} = {} & A_{3m}^{(1)}(\cosh\sigma_1\tau-\cosh\sigma_m\tau)+A_{3m}^{(2)}(\cosh 3\sigma_1\tau-\cosh\sigma_m\tau) \\ & +\sum_n A_{3mn}^{(3)}(\cosh(\sigma_1-\sigma_n)\tau-\cosh\sigma_m\tau) \\ & +\sum_n A_{3mn}^{(4)}(\cosh(\sigma_1+\sigma_n)\tau-\cosh\sigma_m\tau), \quad (3.14a)\end{aligned}$$

$$\begin{aligned}b_{3m} = {} & B_{3m}^{(1)}\left(\sinh\sigma_1\tau-\frac{\sigma_1}{\sigma_m}\sinh\sigma_m\tau\right)+B_{3m}^{(2)}\left(\sinh 3\sigma_1\tau-3\frac{\sigma_1}{\sigma_m}\sinh\sigma_m\tau\right) \\ & +\sum_n B_{3mn}^{(3)}\left(\sinh(\sigma_1-\sigma_n)\tau-\frac{(\sigma_1-\sigma_n)}{\sigma_m}\sinh\sigma_m\tau\right) \\ & +\sum_n B_{3mn}^{(4)}\left(\sinh(\sigma_1+\sigma_n)\tau-\frac{\sigma_1+\sigma_n)}{\sigma_m}\sinh\sigma_m\tau\right)+B_{3m}^{(5)}\frac{\sinh\sigma_m\tau}{\sigma_m}, \quad (3.14b)\end{aligned}$$

where $A_{3m}^{(1)}$, $A_{3m}^{(2)}$, $A_{3mn}^{(3)}$, $A_{3mn}^{(4)}$ and $B_{3m}^{(1)}$, $B_{3m}^{(2)}$, $B_{3mn}^{(3)}$, $B_{3mn}^{(4)}$, $B_{3mn}^{(5)}$ are constants (given in Appendix B).

4. The inner solution

The solution of the previous section is valid so long as the expansions representing the solution remain ordered. As the parameter K is allowed to approach 1 a point is reached where this is no longer true. More precisely, as soon as $K^2-1=O(\epsilon^2)$, the second term in (3.2c) is the same size as the first. If we let $K^2-1=O(\epsilon^2)$, then

$\sigma_1 = T(1-K^2)^{\frac{1}{2}} = O(\epsilon)$, $a_1 \sim \epsilon \cosh \sigma_1 t = O(\epsilon)$, $b_1 \sim \epsilon(\sigma_1/T)\sinh \sigma_1 t = O(\epsilon^2)$, and $\mathrm{d}/\mathrm{d}\tau \sim \sigma_1 = O(\epsilon)$. These results suggest the following inner expansions:

$$K^2 = 1+\epsilon^2\alpha+\ldots, \tag{4.1a}$$

$$a_n = \epsilon\delta_{n1}a_{11}(t_1)+\epsilon^2 a_{2n}(t_1)+\ldots, \tag{4.1b}$$

$$b_n = \epsilon^2\delta_{n1}b_{21}(t_1)+\epsilon^3 b_{3n}(t_1)+\ldots, \tag{4.1c}$$

$$t_1 = \epsilon t. \tag{4.1d}$$

After substituting these expansions into (2.8) we obtain at leading order

$$\dot{a}_{11}-Tb_{21} = 0, \tag{4.2a}$$

$$\dot{b}_{21}+\alpha a_{11} = \tfrac{1}{2}a_{11}^3 E_{1111}. \tag{4.2b}$$

After eliminating b_{21} we obtain

$$\ddot{a}_{11}+\alpha T a_{11} = \tfrac{1}{2}Ta_{11}^3 E_{1111}, \tag{4.3}$$

which is subject to the following initial conditions:

$$a_{11}(0) = 1, \quad \dot{a}_{11}(0) = 0, \tag{4.4a, b}$$

The solution of this initial-value problem is (Davis 1962, pp. 207–209)

$$a_{11} = \mathrm{cn}\,(\lambda t_1 \,|\, m), \tag{4.5a}$$

where

$$\lambda^2 = T(\alpha-\tfrac{1}{2}E_{1111}), \tag{4.5b}$$

$$m = -\frac{\tfrac{1}{2}E_{1111}}{(\alpha-\tfrac{1}{2}E_{1111})}, \tag{4.5c}$$

and cn is a Jacobian elliptic function. When $\alpha > \frac{1}{2}E_{1111}$ the solution exhibits oscillatory behaviour, thus the system is stable. On the other hand, when $\alpha < \frac{1}{2}E_{1111}$ the solution grows without bound implying instability. Therefore, $\alpha = \frac{1}{2}E_{1111}$ defines cutoff and

$$K_c^2 = 1+\tfrac{1}{2}\epsilon^2 E_{1111} \tag{4.6}$$

gives the nonlinear correction to the cutoff wavenumber.

Letting $\alpha \to \pm\infty$ we find

$$m = -\frac{E_{1111}}{2\alpha}+O\left(\frac{1}{\alpha^2}\right) \tag{4.7}$$

$$\lambda t_1 = \mathrm{i}\sigma_1 t+O\left(\frac{1}{\alpha}\right), \tag{4.8}$$

where $\mathrm{i} = \sqrt{-1}$. Using

$$\mathrm{cn}\,(u\,|\,m) = \cos u+O(m) \quad \text{as } m\to 0 \tag{4.9}$$

we then find

$$a_{11} = \cosh \sigma_1 t+O\left(\frac{1}{\alpha}\right) \tag{4.10}$$

which matches to the outer solution at order-ϵ.

5. The eigenfunctions

The solutions in the preceding two sections were found without specifying the cross-sectional geometry. In this section we consider two geometries. The particular eigenfunctions ψ_n for these geometries are then given.

5.1. *Rectangular geometry*

Say that we want to consider the instability in a container of rectangular cross-section with sides of lengths X' and Y'. We define

$$\boldsymbol{x} = (x, y), \quad S = \{(x, y): 0 \leqslant x \leqslant X, 0 \leqslant y \leqslant Y\}, \tag{5.1a, b}$$

where

$$X = X'k', \quad Y = Y'k'. \tag{5.2a, b}$$

The corresponding eigenfunctions are then

$$\psi_i = c_{mn} \cos\frac{m\pi}{X}x \cos\frac{n\pi}{Y}y \quad (m = 0, 1, 2, 3, \ldots, \quad n = 0, 1, 2, 3, \ldots). \tag{5.3}$$

and the c_{mn} are normalizing constants given by

$$c_{mn} = \frac{2}{[(1+\delta_{0m})(1+\delta_{0n})]^{\frac{1}{2}}}. \tag{5.4}$$

Because of the limited types of interactions allowed in this weakly nonlinear analysis, we need only consider a fraction of the set given above. We need only consider modes n such that C_{n11} or $C_{n111} \neq 0$. If we seek a solution with primary-mode indices (p, q) (i.e. an initial condition with $m = p$ and $n = q$) so that

$$\psi_1 = c_{pq} \cos\frac{p\pi}{X}x \cos\frac{q\pi}{Y}y = c_{pq} \cos\frac{L}{(L^2+1)^{\frac{1}{2}}}x \cos\frac{1}{(L^2+1)^{\frac{1}{2}}}y, \tag{5.5}$$

then we need only consider

$$\psi_i = c_{mn} \cos\frac{mL}{(L^2+1)^{\frac{1}{2}}}x \cos\frac{n}{(L^2+1)^{\frac{1}{2}}}y \quad (m = 1, 2, 3 \quad n = 1, 2, 3), \tag{5.6}$$

where

$$L = \frac{k'_x}{k'_y} \tag{5.7}$$

is an aspect ratio.

5.2. *Hexagonal instability*

The hexagonal instability is a member of the rectangular geometry with the following primary mode (Chandrasekhar 1961, pp. 47–50):

$$\psi_1 = \sqrt{\frac{2}{3}}\left[2 \cos\tfrac{1}{2}x \cos\frac{\sqrt{3}}{2}y + \cos x\right]. \tag{5.8a}$$

Again because of the limited interactions that are allowed in this analysis, the only other modes that we need to consider are

$$\psi_2 = 1, \tag{5.8b}$$

$$\psi_3 = \sqrt{\tfrac{2}{3}}[2 \cos x \cos\sqrt{3}y + \cos 2x], \tag{5.8c}$$

$$\psi_4 = \sqrt{\frac{2}{3}}\left[2 \cos\tfrac{3}{2}x \cos\frac{\sqrt{3}}{2}y + \cos\sqrt{3}y\right], \tag{5.8d}$$

$$\psi_5 = \sqrt{\frac{2}{3}}\left[2 \cos\tfrac{3}{2}x \cos\frac{3\sqrt{3}}{2}y + \cos 3x\right], \tag{5.8e}$$

$$\psi_6 = \frac{2}{\sqrt{3}}\left[\cos\tfrac{5}{2}x \cos\frac{\sqrt{3}}{2}y + \cos 2x \cos\sqrt{3}y + \cos\tfrac{1}{2}x \cos\frac{3\sqrt{3}}{2}y\right]. \tag{5.8f}$$

5.3. *Circular geometry*

We now consider the instability in a circular container of radius R'. In this geometry

$$\boldsymbol{x} = (r, \theta), \quad S = \{(r, \theta): \ 0 \leqslant r \leqslant R, \quad 0 \leqslant \theta < 2\pi\}, \tag{5.9a, b}$$

where

$$R = R'k'. \tag{5.10}$$

The complete set of eigenfunctions is then

$$\psi_i = c_{mn} \cos(m\theta) J_m(k_{mn} r) \quad (m = 0, 1, 2, 3, \ldots, \quad n = 1, 2, 3, 4, \ldots), \tag{5.11}$$

where c_{mn} are normalizing constants given by

$$c_{mn} = \frac{\sqrt{2}}{\{(1+\delta_{0m})[1-(m/k_{mn}R)^2]\}^{\frac{1}{2}} J_m(k_{mn}R)}, \tag{5.12}$$

and k_{mn} are determined from

$$J'_m(k_{mn}R) = 0. \tag{5.13}$$

Like the rectangular modes, this set can be reduced. If we seek a solution with the primary mode

$$\psi_1 = c_{pq} \cos(p\theta) J_p(k'_{pq} r'), \tag{5.14}$$

where k'_{pq} satisfies $J'_p(k'_{pq}R') = 0$, then we need only consider

$$m = 0, p, 2p, 3p, \quad n = 1, 2, 3, \ldots.$$

Note that, because products of Bessel functions do not possess the orthogonality properties of circular functions, the radial index must cover the entire range. The series must be truncated at some point in order to obtain numerical results. In the results given here, only modes n such that

$$C_{n11} \geqslant 5 \times 10^{-5} \quad \text{or} \quad C_{n111} \geqslant 5 \times 10^{-3}$$

were retained in the solution.

The asymptotic solutions require evaluating the integrals C_{lmn}, C_{jlmn}, D_{lmn}, D_{jlmn} and E_{jlmn}; though, if use is made of (2.11 *a–d*), we need only evaluate C_{lmn}, C_{jlmn} and E_{jlmn}. In the rectangular geometry these integrals are easily solved analytically. However, in the circular geometry one obtains integrals of products of three or four Bessel functions, which, having no simple solution, must be solved numerically. A very efficient and accurate Gaussian integration scheme was used for this evaluation (see Jacobs 1986 for details).

6. Results and discussion

6.1. *Nonlinear correction to the cutoff wavenumber*

The analysis of §4 gives the expression

$$K_c^2 = 1 + \epsilon^2 \alpha_c, \tag{6.1}$$

where

$$\alpha_c = \tfrac{1}{2} E_{1111}. \tag{6.2}$$

The primary mode of the two-dimensional instability is

$$\psi_1 = \sqrt{2} \cos x. \tag{6.3}$$

Using (2.9*e*) and (4.6) we find for this geometry

$$E_{1111} = \tfrac{3}{2} \tag{6.4}$$

and

$$\alpha_{c,2D} = \tfrac{3}{4}. \tag{6.5}$$

In this analysis we define ϵ as the r.m.s. surface slope. If instead, we had defined ϵ^* as the amplitude of the surface slope we would obtain (for the two-dimensional instability)

$$K_c^2 = 1 + \tfrac{3}{8}\epsilon^{*2} \tag{6.6}$$

which is in agreement with Nayfeh (1969).

Similarly, it is easy to show that for the rectangular three-dimensional instability

$$\alpha_{c,\mathrm{rect}} = \frac{(9L^4 + 2L^2 + 9)}{8(L^2+1)^2}. \tag{6.7}$$

Here, $\alpha_{c,\mathrm{rect}}$ has a maximum at $L = 0$ (or $L = \infty$) with $\alpha_{c,L=0} = \frac{9}{8}$ and a minimum at $L = 1$ with $\alpha_{c,L=1} = \frac{5}{6}$. Note that $\alpha_{c,L=0} \neq \alpha_{c,2D}$, indicating that the two-dimensional solution is not recovered when the aspect ratio in the rectangular solution is allowed to approach zero (or infinity). This is because the rectangular solution is three-dimensional for all values of L. A similar result was obtained by Verma & Keller (1962) on the subject of three-dimensional water waves.

The calculation for the hexagonal disturbance yields

$$\alpha_{c,\mathrm{hex}} = \tfrac{3}{4}. \tag{6.8}$$

Rayleigh–Taylor instability can be viewed as a bifurcation problem with K serving as the bifurcation parameter. The linear stability analysis gives a bifurcation point at $K_c = 1$, and the analysis of §4 gives the first approximation for the behaviour of the branch near $\epsilon = 0$:

$$K_c = 1 + \tfrac{1}{2}\epsilon^2\alpha_c. \tag{6.9}$$

Note that when on the stable side of the critical point ($K > 1$), a disturbance of large enough amplitude will produce instability. Thus, $K = 1$ is a subcritical bifurcation point. Also note that, the larger α_c is, the smaller the amplitude ϵ has to be to produce instability. This implies that geometries with large α_c are preferred, in a sense, over ones with smaller α_c, and that disturbances with long thin shape are preferred over other rectangular modes. This preference is also illustrated by the fact that at $K = 1$ the growth rate of the inner solution is proportional to $\alpha_c^{\frac{1}{2}}$.

The parameter α_c was calculated for several primary modes in the circular geometry, where the primary mode is given by

$$\psi_1 = c_{mn} \cos(m\theta) J_m(k'_{mn} r').$$

These calculations were done numerically for $m = 1, \ldots, 4$ and $n = 1, \ldots, 20$ and are listed in table 1. Note that for fixed m, α_c increases with increasing n. In fact it is easy to show that α_c increases like $\ln(n)$ as $n \to \infty$. Physically, letting n approach infinity with m fixed, is equivalent to letting L approach zero in the rectangular geometry. That is, the instability is made to get longer and thinner as n increases. These results reinforce those in the rectangular geometry, namely that long thin shapes are preferred over those more equally proportioned.

6.9. *Growth of the nonlinear instability*

The instability described by the outer solution consists initially of a single normal mode (the 'primary' mode). For small enough ϵ, the amplitude of this mode is dominated by the first-order solution a_{11} (linear theory). However, as the amplitude

n	$m=0$	$m=1$	$m=2$	$m=3$	$m=4$
1	—	0.657251	0.630663	0.733122	0.845801
2	0.775767	0.944832	0.795445	0.780701	0.797300
3	0.981026	1.174957	0.969848	0.912120	0.894380
4	1.113995	1.340140	1.106575	1.025345	0.988038
5	1.212352	1.468444	1.217686	1.121553	1.071397
6	1.290374	1.573192	1.310983	1.204569	1.145304
7	1.355015	1.661649	1.391288	1.277371	1.211312
8	1.410186	1.738176	1.461733	1.342108	1.270795
9	1.458303	1.805597	1.524448	1.400344	1.324852
10	1.500962	1.865841	1.580950	1.453241	1.374349
11	1.539274	1.920284	1.632348	1.501680	1.419970
12	1.574041	1.969944	1.679483	1.546344	1.462264
13	1.605864	2.015589	1.723003	1.587772	1.501671
14	1.635202	2.057820	1.763422	1.626397	1.538554
15	1.662414	2.097110	1.801148	1.662570	1.573212
16	1.687787	2.133842	1.836518	1.696582	1.605893
17	1.711554	2.168327	1.869807	1.728674	1.636808
18	1.733906	2.200825	1.901246	1.759049	1.666136
19	1.755002	2.231552	1.931028	1.787882	1.694030
20	1.774976	2.260690	1.959319	1.815320	1.720623

TABLE 1. α_c as a function of m and n in the circular geometry

increases the effects of the nonlinearities begin to emerge. Energy is fed, via the quadratic and cubic nonlinearities to harmonics (or secondary modes). The addition of these harmonics in the solution causes the basic shape of the interface to change. In addition, the interaction of the secondary modes with the primary (and in some cases the interaction of the primary mode with itself) causes the growth of the primary mode to be modified. This modification, unlike the linear solution, is a function of geometry and can be used to determine how geometry effects the growth of the instability. This information also provides a means to predict which types of shapes will be selected in a real system.

Figure 1 is a plot of the primary-mode amplitude a_1 of the two-dimensional instability as a function of time with $\epsilon = 0.1$, $K = 0$ (no surface tension), and $d = \infty$ (infinite depth). Also plotted in this figure is a dashed line representing linear theory. This plot is typical of all geometries considered for these parameter values and is presented here to illustrate the general behaviour of the nonlinear solutions which follow. Initially, the nonlinear solution shown in figure 1 closely follows linear theory. As the amplitude increases, the curve begins to fall below the dashed line. This continues until a point of maximum amplitude is reached, after which the nonlinear solution decreases rapidly. The relative size of the components a_{21} and a_{31} with respect to a_{11} is indicated by the distance separating the linear and nonlinear solutions. When this distance becomes large, the asymptotic series have broken down and the solution is invalid. We know from earlier experimental observations (Lewis 1950 and Emmons *et al.* 1960) that, as $t \to \infty$, the growth of surface elevation should asymptotically approach that of constant acceleration in the crests ($\eta \sim t^2$), and constant velocity in the troughs ($\eta \sim t$). This indicates that $\mathrm{d}^2 a_1/\mathrm{d}t^2$ should always be positive. Since negative curvature in this plot is clearly unrealistic, the inflexion point in the nonlinear solution curve can be viewed as the limit of validity of the solution. The nonlinear solutions in the following figures will be plotted up to the inflexion point.

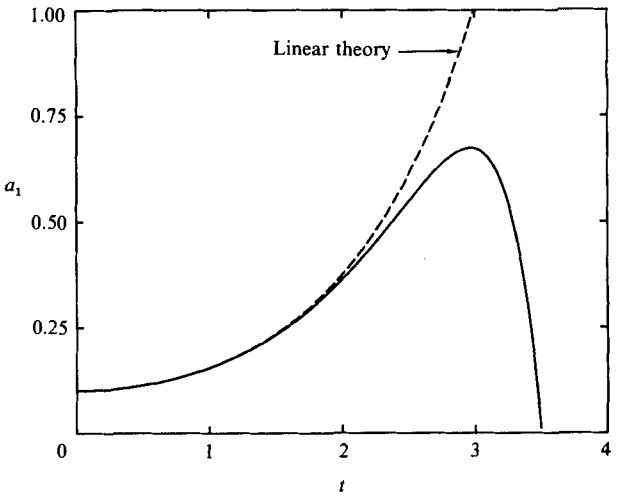

FIGURE 1. Primary-mode amplitude versus time of the two-dimensional instability with $\epsilon = 0.1$, $K = 0$ and $d = \infty$. The dashed line is linear theory.

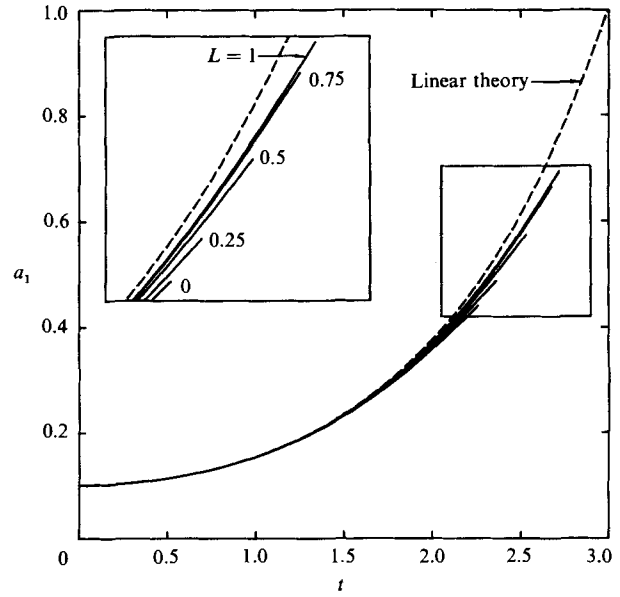

FIGURE 2. Primary-mode amplitude versus time of the rectangular instability with $\epsilon = 0.1$, $K = 0$, $d = \infty$ and several aspect ratios. The dashed line is linear theory.

Figure 2 is a plot of the primary-mode amplitude a_1 as a function of time for several rectangular instabilities. Given in this plot are solutions with aspect ratios $L = 1$, 0.75, 0.5, 0.25 and 0. These were again calculated with $\epsilon = 0.1$, $K = 0$ and $d = \infty$. As in the preceding figure, the curves initially follow linear theory, then begin to fall below the dashed line as the amplitude increases. In addition, the solutions themselves begin to diverge and the effect of geometry becomes apparent. The figure contains solutions of the rectangular instability with a number of aspect ratios, and illustrates the dependence of the rate of growth of the nonlinear instability on aspect ratio. This plot shows that the rate of growth is monotonic with respect to aspect

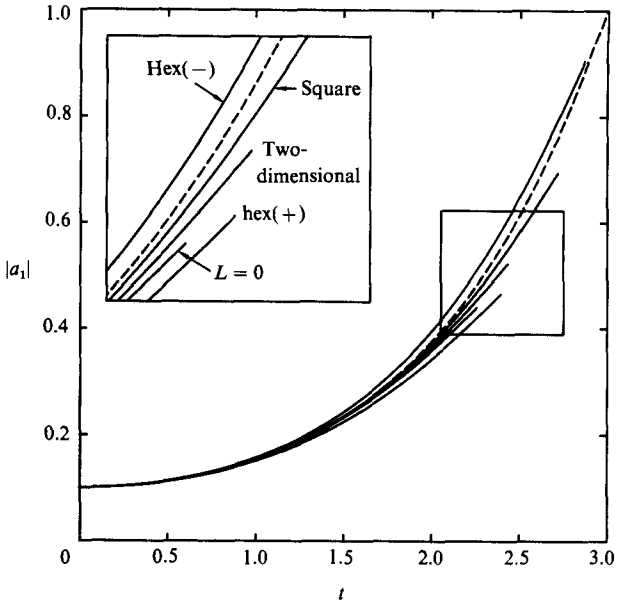

FIGURE 3. Primary-mode amplitude versus time of the hexagonal, square, two-dimensional and zero-aspect-ratio instabilities with $\epsilon = 0.1$, $K = 0$ and $d = \infty$. The dashed line is linear theory.

ratio and that the instability with $L = 1$ grows fastest and $L = 0$ grows slowest. The results indicate a preference toward an instability of square shape over other rectangular modes.

Figure 3 is a plot of the primary coefficient as a function of time of the hexagonal instability. Also given in this figure are the solutions of both the square and the two-dimensional instability. As in figure 2 these solutions were calculated with $\epsilon = 0.1$, $K = 0$ and $d = \infty$. The hexagonal instability possesses unique characteristics which are immediately apparent in the figure. Note that there are two separate hexagonal solutions in this plot. One is labelled hex (+), the other hex (−), where the (+) or (−) indicate the sign of the initial amplitude. The hexagonal (+) pattern consists of grid of hexagonal cells oriented with crests in the centre of the cells and troughs at the cell boundaries. The hexagonal (−) pattern consists of grid of hexagonal cells oriented with troughs in the centre of the cells and crests at the cell boundaries. The hexagonal instability is unique in that a change in sign of the initial amplitude changes the solution in a non-trivial way. Changing the sign of ϵ in a rectangular instability is equivalent to multiplying the entire solution by -1 (i.e. $a_1(t; -\epsilon) = -a_1(t; \epsilon)$); whereas in the hexagonal pattern, a change of sign cannot be resolved in this manner.

Figure 3 shows that the hexagonal instability oriented with troughs at the cell centres grows significantly faster than the one with the opposite orientation. This is because C_{111} (and therefore a_{12}) is non-zero, making the hexagonal instability the only solution in the rectangular geometry in which terms quadratic in ϵ appear in the primary coefficient. Thus, growth is enhanced with the right choice of the sign of ϵ; and consequently the hexagonal disturbance grows faster than the square, two-dimensional, or any other pattern in the rectangular geometry. Also, note that the growth of the hexagonal (−) solution exceeds linear theory for a good portion of its evolution.

Figure 4 contains plots of the hexagonal, square, two-dimensional and zero-

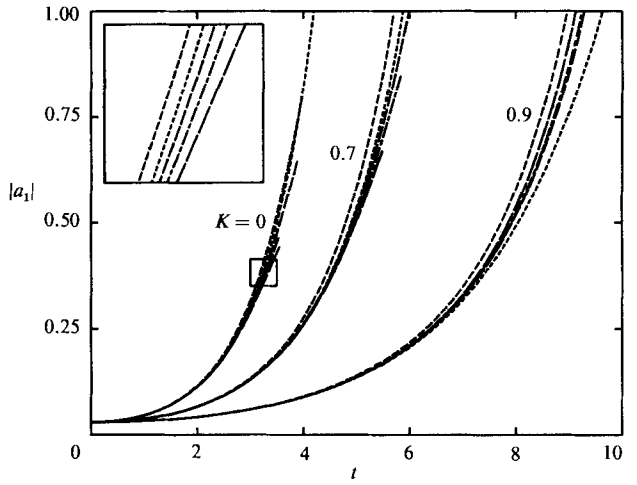

FIGURE 4. Primary-mode amplitude versus time of the hexagonal, square, two-dimensional and zero-aspect-ratio instabilities with $\epsilon = 0.03$, $d = \infty$ and various K. ----, hex (−); ——, square; ——, $L = 0$; – – – –, two-dimensional; ·····, linear theory.

L	$K = 0$	$K = 0.3$	$K = 0.6$	$K = 0.9$
0	0.492933	0.437235	0.461497	0.549582
0.1	0.434123	0.441203	0.464929	0.552123
0.2	0.440154	0.446633	0.468772	0.553264
0.3	0.447269	0.452923	0.472732	0.552347
0.4	0.454550	0.459337	0.476486	0.548759
0.5	0.461185	0.465199	0.479744	0.543249
0.6	0.466642	0.470043	0.482243	0.537570
0.7	0.470690	0.473655	0.484745	0.533103
0.8	0.473344	0.476032	0.485752	0.530161
0.9	0.474768	0.477311	0.486386	0.528631
1.0	0.475190	0.477690	0.486576	0.528187

TABLE 2. $a_1(t^+)$ as a function of L and K for the rectangular instability with $\epsilon = 0.03$

aspect-ratio instabilities calculated with three different values of K, illustrating the effect of surface tension on the growth of the nonlinear instability. These solutions were calculated using $\epsilon = 0.03$ and $d = \infty$ with $K = 0, 0.7, 0.9$. The figure shows that increasing K amplifies the growth of the nonlinear solutions, and that this amplification affects the hexagonal instability to a greater extent than the other modes. Note that when $K \leqslant 0.7$ the ranking with respect to rates of growth of the different instabilities is uniform. In this range, hexagonal (−) always grows fastest followed by the square, two-dimensional and zero-aspect-ratio instabilities. However when $K = 0.9$ this order changes, where at that point hexagonal (−) still grows fastest, with $L = 0$ second, followed by the two-dimensional and square instabilities.

Table 2 gives the primary amplitude a_1 of the rectangular instability as a function of aspect ratio L and the parameter K. In this table the amplitudes are taken at time t^+, given by

$$\epsilon a_{11}(\sigma_1 t^+) = \tfrac{1}{2}. \tag{6.10}$$

The table shows that in the range $0 \leqslant K \leqslant 0.6$, the rectangular instability with $L = 1$ grows fastest, but when $K = 0.9$ preference shifts towards the modes with

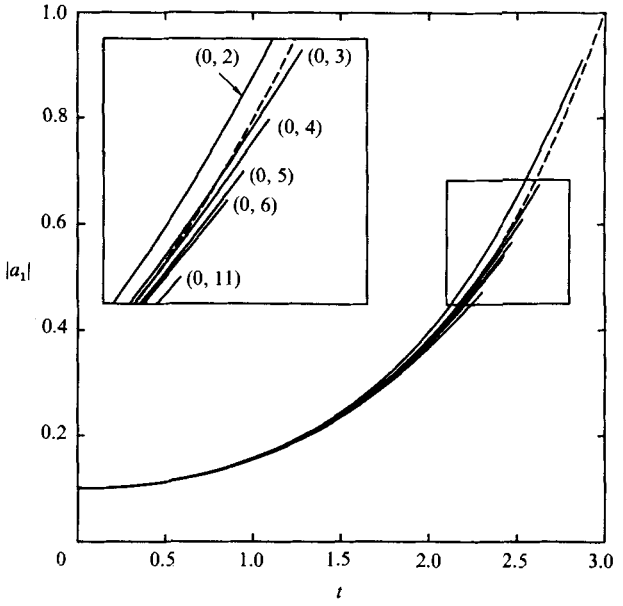

FIGURE 5. Primary-mode amplitude versus time of several axisymmetric (−) instabilities with $\epsilon = 0.1$, $K = 0$ and $d = \infty$. The dashed line is linear theory.

lower aspect ratio. Recall that near the cutoff wavenumber, we found the rectangular mode with $L = 0$ to be the most unstable. Thus in the limit as $K \to 1$, the results of the outer solution appear to be in agreement with those of the inner solution.

Like the hexagonal instability, the circular axisymmetric instability has terms, quadratic in ϵ, which appear in the primary-mode expansions, and thus shows sensitivity to the sign of the initial amplitude. Figure 5 is a plot of the primary coefficient as a function of time for several axisymmetric modes. Given in this plot are the solutions with primary-mode indices $\{(0, n): n = 2, 3, 4, 5, 6, 11\}$, oriented so that the point $r = 0$ is a trough (axisymmetric (−)). These solutions were calculated using $\epsilon = 0.1$, $K = 0$ and $d = \infty$. Figure 6 gives solution curves for the same initial modes as figure 5 but oriented with a crest at $r = 0$ (axisymmetric (+)). In the first figure, the solution with index (0, 2) dominates the other modes, with the rate of growth decreasing monotonically with increasing radial-mode index. In the corresponding solutions with centre crests, no single mode dominates. Instead all the curves are more or less grouped together, though the rate of growth seems to decrease steadily with increasing n when n is large. For low radial-mode index, the instabilities with centre troughs grow significantly faster than the ones with centre crests. This difference decreases with increasing n.

Intuitively one might expect the axisymmetric solution to converge to the Cartesian two-dimensional solution as the radial-mode number approaches infinity; however, that does not appear to be the case. The solution with highest mode index (i.e. $n = 11$) has already fallen below the two-dimensional solution; and in fact, it appears that the solution does not converge at all. The reason for this lies in the fact that like E_{1111} the integrals C_{1111} and D_{1111} do not converge as $n \to \infty$.

Solutions of another set of circular modes are given in figure 7. The primary coefficient of modes with indices $\{(1, n): n = 1, 2, 3, 4, 5, 10\}$ are plotted in this figure, calculated using the same parameter values as the preceding two figures. Note that, although these instabilities do not share the property of dependence upon the sign of

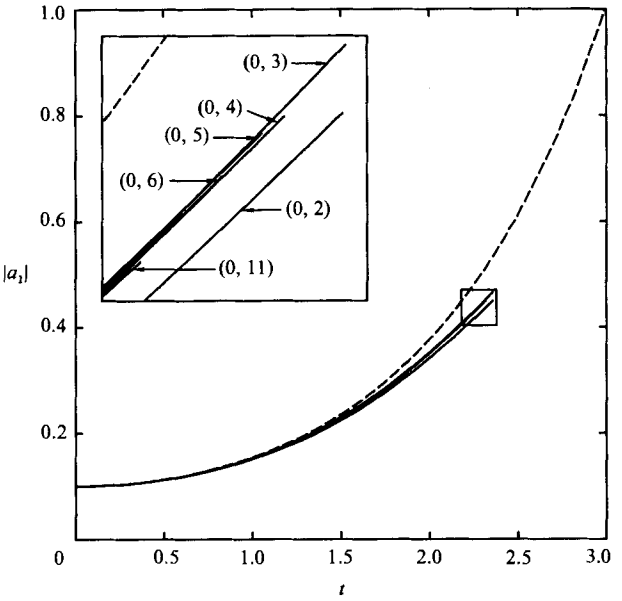

FIGURE 6. Primary-mode amplitude versus time of several axisymmetric (+) instabilities with $\epsilon = 0.1$, $K = 0$ and $d = \infty$. The dashed line is linear theory.

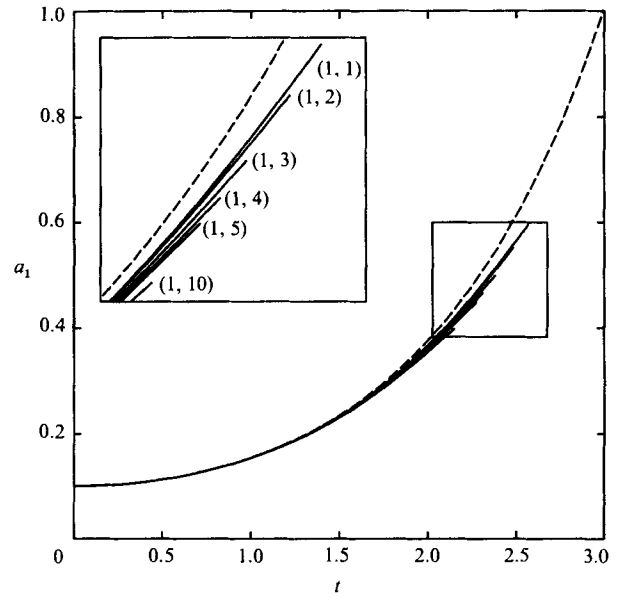

FIGURE 7. Primary-mode amplitude versus time of several circular instabilities with $m = 1$ and with $\epsilon = 0.1$, $K = 0$ and $d = \infty$. The dashed line is linear theory.

the initial amplitude, they do share the characteristic that the rate of growth decreases with increasing radial mode index. Again, one might expect the circular non-axisymmetric solutions to converge to the zero-aspect ratio rectangular solution as $n \to \infty$; however, like the axisymmetric solutions, that does not appear to be the case.

m	$n=1$	$n=2$	$n=3$	$n=4$	$n=5$	$n=6$	$n=7$
0	—	0.5169	0.4822	0.4708	0.4590	0.4522	(0.4452)
1	0.4589	0.4489	0.4347	0.4240	0.4154	0.4083	0.4023
2	0.4669	0.4600	0.4493	0.4404	0.4331	(0.4269)	0.4214
3	0.4627	0.4614	0.4533	0.4460	0.4397	0.4342	0.4293
4	0.4568	0.4605	0.4546	0.4486	(0.4431)	0.4382	0.4338
5	0.4505	0.4588	0.4546	0.4497	0.4450	0.4406	0.4366
6	0.4441	0.4567	0.4540	0.4500	0.4460	0.4421	0.4385
7	0.4378	0.4543	0.4530	(0.4499)	0.4464	0.4430	0.4397
8	0.4315	0.4518	0.4518	0.4494	0.4464	0.4434	0.4405
9	0.4254	0.4493	(0.4504)	0.4487	0.4462	0.4436	0.4409
10	0.4194	0.4467	0.4489	0.4478	0.4458	0.4435	0.4411
11	0.4135	0.4442					
12	0.4078	0.4416					
13	0.4021	(0.4390)					
14	0.3966	0.4365					
15	0.3912	0.4339					
16	0.3858						
17	(0.3805)						
18	0.3753						

TABLE 3. $a_1(t^+)$ for several circular modes with $\epsilon = 0.01$ and $K = 0$

(m, n)	R	$K=0$	$K=0.3$	$K=0.6$	$K=0.9$
(0, 7)	19.6159	0.445192	0.455354	0.487067	0.593089
(2, 6)	19.5129	0.426860	0.436794	0.467403	0.568316
(4, 5)	19.1960	0.433139	0.450663	0.474580	0.557970
(7, 4)	19.9419	0.449868	0.456449	0.477499	0.551952
(9, 3)	19.0046	0.450399	0.456925	0.477682	0.550929
(13, 2)	19.8832	0.439015	0.447156	0.472775	0.561071
(17, 1)	19.1045	0.380478	0.396792	0.447945	0.616927

TABLE 4. $a_1(t^+)$ as a function of K for the circular modes with $19 < R < 20$ and with $\epsilon = 0.01$

In the rectangular geometry we learned that when $K = 0$, the rectangular instability with $L = 1$ grows faster than any other rectangular mode. One would expect a similar preference in the circular geometry. This implies that for large m and n the fastest growing modes should lie on some diagonal of (m, n)-space (i.e. $m \sim n$ as $m, n \to \infty$). Table 3 gives values of $a_1(t^+)$ for a number of circular modes. Near $(m, n) = (0, 1)$, the axisymmetric modes grow faster than the others; however, sufficiently far from the origin it appears that the instabilities that grow the fastest lie on a line passing through the indices (3, 2) and (9, 3). Each mode in table 3 has associated with it a value of the dimensionless radius R. In comparing different instabilities in the circular geometry one should compare modes with the same wavenumber and which exist in an enclosure with the same radius. Moving out from the origin is the same as increasing R. The change in R occurs in discrete jumps; however, when R is large, these jumps are relatively small. Marked in table 3 are seven modes with nearly equal R (i.e. $19 < R < 20$). It is evident that the mode (9, 3) has a larger value of $a_1(t^+)$ than any other mode in this set. Table 4 illustrates the effect of surface tension on the growth of the seven modes marked in table 3, and shows that when $K = 0$ the mode (9, 3) has a slight advantage over the others. This

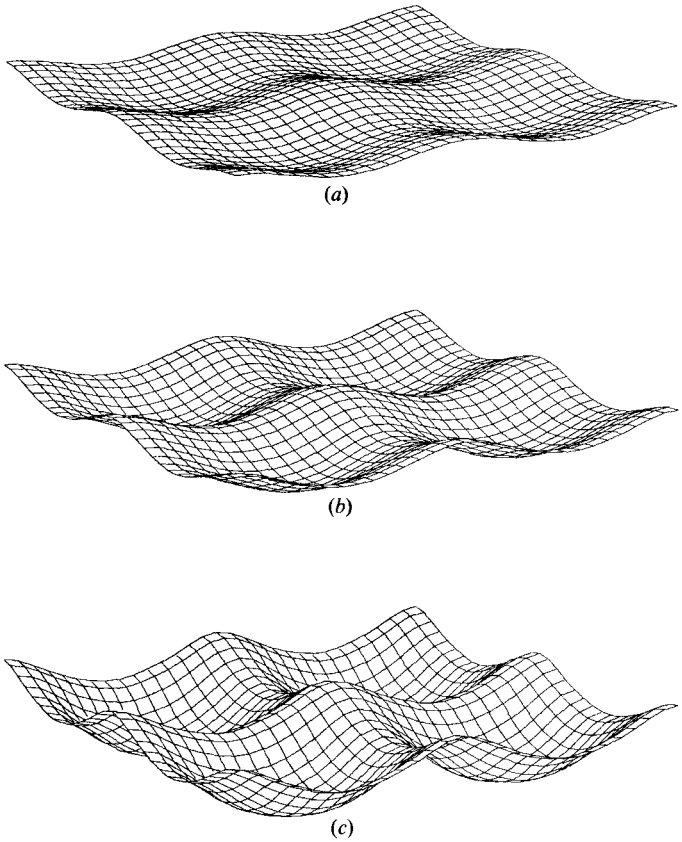

FIGURE 8. Three views of the square instability with $\epsilon = 0.1$, $K = 0$ and $d = \infty$. (a) $t = 1.5$, $a_1 = 0.2341$; (b) $t = 2.0$, $a_1 = 0.3703$; (c) $t = 2.5$, $a_1 = 0.5809$.

advantage is maintained at $K = 0.3$; however when K is increased the lead shifts towards the modes on each end of the column. At $K = 0.9$ the mode (17, 1) grows faster than the others. The table shows the expected result that when $K = 0$ modes with aspect ratio near 1 grow faster than those with longer thinner shape; however near $K = 1$, modes with zero aspect ratio dominate.

Figure 8 gives three consecutive views of the square instability at $t = 1.5$, 2.0 and 2.5. This solution was calculated with $\epsilon = 0.1$, $K = 0$ and $d = \infty$. Shown in this figure are two wavelengths in both the x- and y-directions, thus providing a view of four square cells. Each of these consists of a trough located at the centre of the cell with crests at each of the four corners. At $t = 1.5$ the solution, for the most part, contains only the primary mode, making the shape nearly sinusoidal in both the x- and y-directions. As time progresses, the higher harmonics begin to be observable and at $t = 2.5$ the effect of nonlinearity on the surface shape is clearly evident. At that point, the troughs have become wider and more spherical, taking on the characteristics of bubbles. In addition, the crests have become sharper. In the latter stages of development (as shown in figure 8*c*), the instability appears as an array of square cells, the centres of which contain nearly spherical bubbles. The boundaries of each cell are defined by sharp two-dimensional crests with larger three-dimensional peaks at each of the four corners.

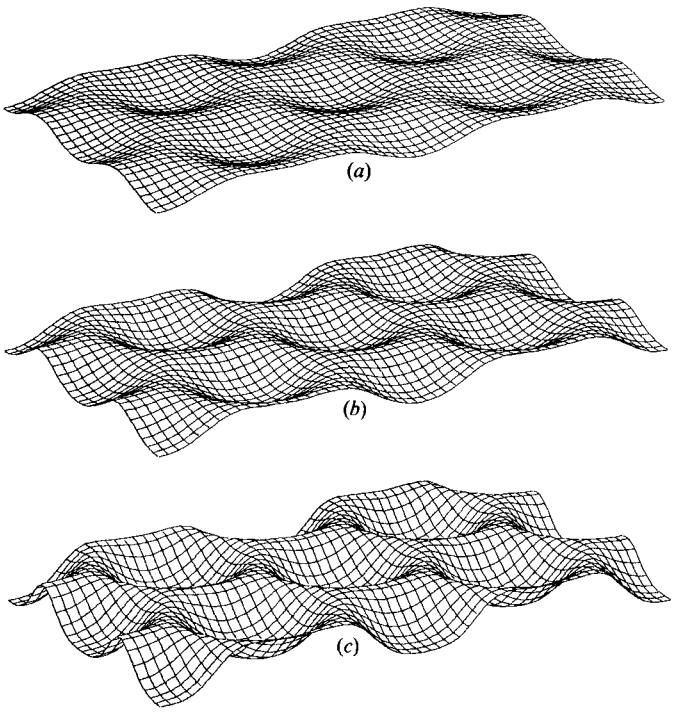

FIGURE 9. Three views of the hexagonal (−) instability with $\epsilon = 0.1$, $K = 0$ and $d = \infty$. (*a*) $t = 1.5$, $a_1 = -0.2431$; (*b*) $t = 2.0$, $a_1 = -0.3958$; (*c*) $t = 2.5$, $a_1 = -0.6478$.

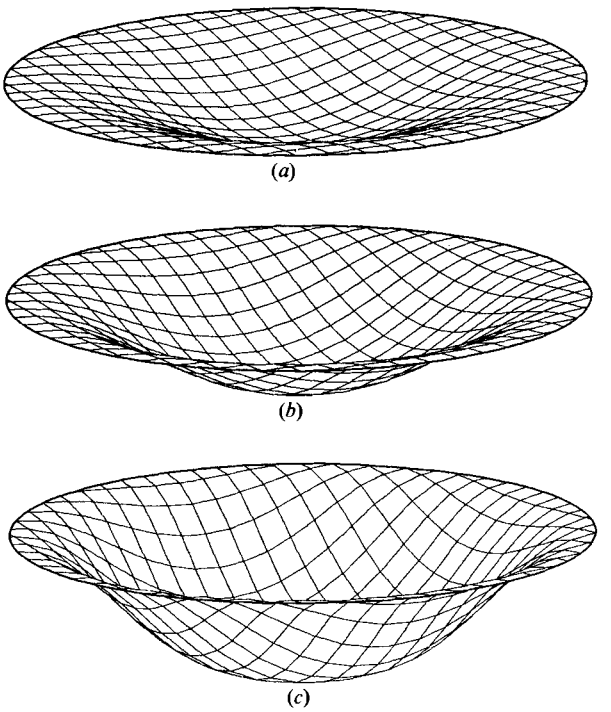

FIGURE 10. Three views of the axisymmetric (−) instability (0, 2) with $\epsilon = 0.1$, $K = 0$ and $d = \infty$. (*a*) $t = 1.5$, $a_1 = 0.2438$; (*b*) $t = 2.0$, $a_1 = 0.3975$; (*c*) $t = 2.5$, $a_1 = 0.6517$.

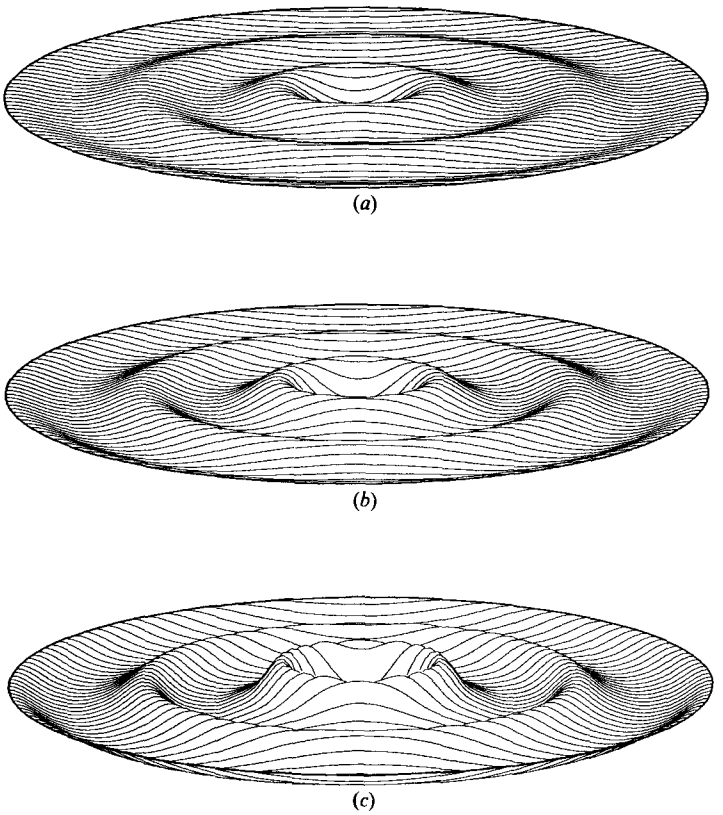

FIGURE 11. Three views of the axisymmetric (−) instability (0, 6) with $\epsilon = 0.1$, $K = 0$ and $d = \infty$. (a) $t = 1.5$, $a_1 = 0.2369$; (b) $t = 2.0$, $a_1 = 0.3745$; (c) $t = 2.5$, $a_1 = 0.5700$.

Figure 9 gives three similar views of the hexagonal (−) instability. Shown in this plot are two wavelengths in both the x- and y-directions. This hexagonal instability is characterized by a hexagonal grid of roughly circular troughs each surrounded by a hexagonal-shaped ridge. Each of these cells is surrounded by six equidistant cells. Like the square instability, at $t = 1.5$ the solution is dominated by the primary mode, making the surface shape sinusoidal in nature. At $t = 2.5$ the higher harmonics are visible. At that point the instability has become a grid of nearly spherical bubbles surrounded by ridges of nearly uniform height outlining the borders of the hexagonal cells.

Figure 10 gives three views of the axisymmetric (−) instability with $n = 2$ again taken at $t = 1.5$, 2.0 and 2.5. Like the others, this solution was calculated with $\epsilon = 0.1$, $K = 0$ and $d = \infty$. At $t = 1.5$ the surface shape is primarily that of the Bessel function $J_0(r)$. Note that as time progresses the centre trough becomes wider and more spherical. Likewise, a narrow crest begins to form near the boundary. If this instability could be viewed for a long enough time, the surface would evolve into a single bubble rising up ('up' meaning opposite to the body force) the tube with a thin film of liquid falling down the edge of the cylinder.

Figure 11 gives a time sequence of another axisymmetric (−) instability, this time with $n = 6$. The instability here takes the form of concentric ring waves. As the effects of the nonlinearities emerge, the crests become sharper and narrower, and the troughs wider, much the same as the two-dimensional instability.

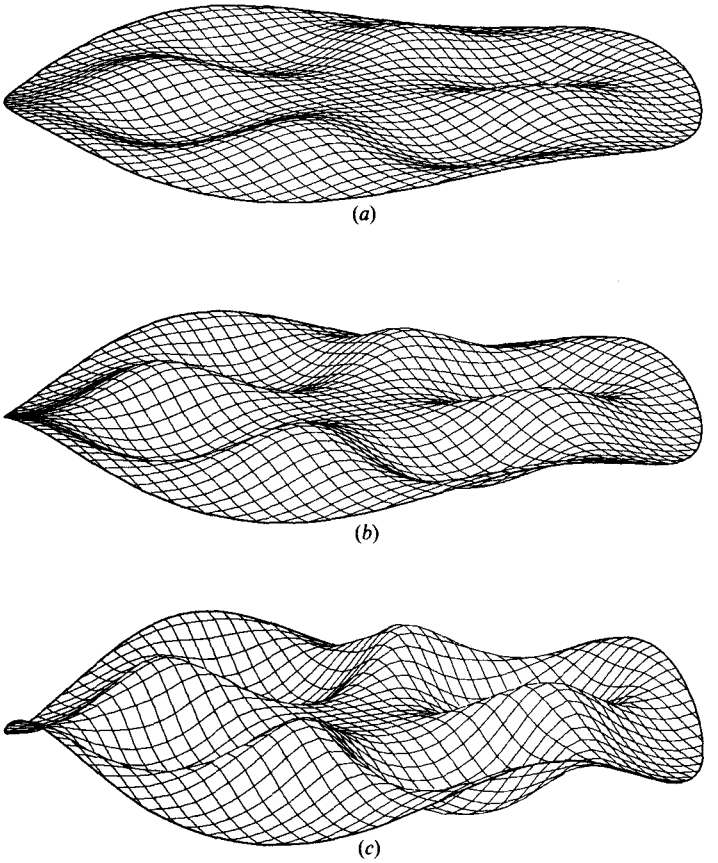

FIGURE 12. Three views of the circular instability (4, 2) with $\epsilon = 0.1$, $K = 0$ and $d = \infty$. (*a*) $t = 1.5$, $a_1 = 0.2339$; (*b*) $t = 2.0$, $a_1 = 0.3687$; (*c*) $t = 2.5$, $a_1 = 0.5710$.

Figure 12 is three views of a circular, fully three-dimensional instability. This solution was calculated with the initial mode (4, 2) and it is one of the modes on the so-called 'diagonal' of mode-index space. In these views, the instability evolves from a more or less sinusoidal shape to one consisting of broad spherical bubbles separated with sharp narrow crests. This solution is different from the others in that the crests are in the shape of triangular pyramids.

7. Summary

We derived a pair of weakly nonlinear asymptotic solutions for three-dimensional Rayleigh–Taylor instability. These solutions were developed assuming an arbitrary plan geometry and then evaluated for several initial surface shapes. In examining the growth of the amplitude of the primary mode, we found that the hexagonal and axisymmetric instabilities grow faster than any of the other types in their respective geometry, and that this advantage increases slightly with increasing K. In addition we found that for low to moderate K, disturbances that are more or less equally proportioned in the lateral directions were favoured; however, as $K \to 1$ the preference shifts toward modes with longer and thinner shape. In viewing the various instabilities we found that the effect of the nonlinearities on surface shape is to

transform the troughs into bubble-like structures as well as to transform crests into ridges or spikes. It is interesting to note that the instabilities displaying the fastest growth in the low to moderate K regime were those that formed spherical bubbles in the later stages of development. For example, the hexagonal (−) and square instabilities form spherical bubbles and were found to grow significantly faster than other rectangular solutions forming long thin troughs such as the two-dimensional or zero-aspect-ratio instabilities. Similarly, the axisymmetric (−) instability with $n = 2$ was also found to grow faster than other solutions that form trough-like bubbles such as the axisymmetric instabilities with high radial-mode index. This evidence suggests that the ability to form spherical bubbles is an important factor in selecting which geometry grows the fastest.

This work was supported by the National Science Foundation under grant MEA 81-05542.

Appendix A. Constants in the forcing functions of the third-order equations (3.11*a*, *b*)

$$P_m^{(1)} = \sum_n \left[\frac{B_{2n}^{(1)}}{2} (k_n^2 C_{m1n} - D_{m1n}) + \frac{\sigma_1}{T} (A_{2n}^{(2)} - \tfrac{1}{2} A_{2n}^{(1)}) (C_{mn1} - D_{mn1}) \right] + \frac{\sigma_1}{4} (\tfrac{1}{2} C_{m111} - D_{m111}),$$

$$P_m^{(2)} = \sum_n \left[\frac{B_{2n}^{(1)}}{2} (k_n^2 C_{m1n} - D_{m1n}) + \frac{\sigma_1 A_{2n}^{(1)}}{2T} (C_{mn1} - D_{mn1}) \right] + \frac{\sigma_1}{4} (\tfrac{1}{2} C_{m111} - D_{m111}),$$

$$P_{mn}^{(3)} = -\frac{B_{2n}^{(2)}}{2} (k_n^2 C_{m1n} - D_{m1n}) - \frac{\sigma_1 (A_{2n}^{(1)} + A_{2n}^{(2)})}{2T} (C_{mn1} - D_{mn1}),$$

$$P_{mn}^{(4)} = \frac{B_{2n}^{(2)}}{2} (k_n^2 C_{m1n} - D_{m1n}) - \frac{\sigma_1 (A_{2n}^{(1)} + A_{2n}^{(2)})}{2T} (C_{mn1} - D_{mn1}),$$

$$Q_m^{(1)} = \sum_n \left[\frac{\sigma_1 B_{2n}^{(1)}}{2T} (D_{m1n} - T\kappa_n C_{mn1}) - \sigma_1^2 (\tfrac{1}{2} A_{2n}^{(1)} + A_{2n}^{(2)}) C_{mn1} \right] + \frac{\sigma_1^2}{4T} (D_{m111} - \tfrac{1}{2} C_{m111}) + \tfrac{3}{8} K^2 E_{m111},$$

$$Q_m^{(2)} = \sum_n \left[-\frac{\sigma_1 B_{2n}^{(1)}}{2T} (D_{m1n} + 3T\kappa_n C_{mn1}) - \frac{\sigma_1^2 A_{2n}^{(1)}}{2} C_{mn1} \right] - \frac{\sigma_1^2}{4T} (D_{m111} + \tfrac{3}{2} C_{m111}) + \tfrac{1}{8} K^2 E_{m111},$$

$$Q_{mn}^{(3)} = \frac{\sigma_1 B_{2n}^{(2)}}{2T} \left(D_{m1n} + \left(1 - \frac{\sigma_n}{\sigma_1} \right) T\kappa_n C_{mn1} \right) + \frac{\sigma_1^2}{2} (A_{2n}^{(1)} + A_{2n}^{(2)}) C_{mn1},$$

$$Q_{mn}^{(4)} = -\frac{\sigma_1 B_{2n}^{(2)}}{2T} \left(D_{m1n} + \left(1 + \frac{\sigma_n}{\sigma_1} \right) T\kappa_n C_{mn1} \right) + \frac{\sigma_1^2}{2} (A_{2n}^{(1)} + A_{2n}^{(2)}) C_{mn1}.$$

Appendix B. Constants in the third-order solution (3.14*a*, *b*)

$$A_{3m}^{(1)} = \frac{\sigma_1 P_m^{(1)} + \kappa_m Q_m^{(1)}}{\sigma_1^2 - \sigma_m^2},$$

$$A_{3m}^{(2)} = \frac{3\sigma_1 P_m^{(2)} + \kappa_m Q_m^{(2)}}{9\sigma_1^2 - \sigma_m^2},$$

$$A_{3mn}^{(3)} = \frac{(\sigma_1 - \sigma_n) P_{mn}^{(3)} + \kappa_m Q_{mn}^{(3)}}{(\sigma_1 - \sigma_n)^2 - \sigma_m^2},$$

$$A_{3mn}^{(4)} = \frac{(\sigma_1 + \sigma_n) P_{mn}^{(4)} + \kappa_m Q_{mn}^{(4)}}{(\sigma_1 + \sigma_n)^2 - \sigma_m^2},$$

$$B_{3m}^{(1)} = \frac{\sigma_1 Q_m^{(1)} + (1 - K^2 k_m^2) P_m^{(1)}}{\sigma_1^2 - \sigma_m^2},$$

$$B_{3m}^{(2)} = \frac{3\sigma_1 Q_m^{(2)} + (1 - K^2 k_m^2) P_m^{(2)}}{9\sigma_1^2 - \sigma_m^2},$$

$$B_{3mn}^{(3)} = \frac{(\sigma_1 - \sigma_n) Q_{mn}^{(3)} + (1 - K^2 k_m^2) P_{mn}^{(3)}}{(\sigma_1 - \sigma_n)^2 - \sigma_m^2},$$

$$B_{3mn}^{(4)} = \frac{(\sigma_1 + \sigma_n) Q_{mn}^{(4)} + (1 - K^2 k_m^2) P_{mn}^{(4)}}{(\sigma_1 + \sigma_n)^2 - \sigma_m^2},$$

$$B_{3m}^{(5)} = Q_m^{(1)} + Q_m^{(2)} + \sum_n (Q_{mn}^{(3)} + Q_{mn}^{(4)}).$$

REFERENCES

Baker, L. & Freeman, J. R. 1981 Heuristic model of the nonlinear Rayleigh–Taylor instability. *Phys. Fluids* **52**, 655–663.

Baker, G. R., Meiron, D. I. & Orzag, S. A. 1980 Vortex simulations of the Rayleigh–Taylor instability. *Phys. Fluids* **23**, 1485–1490.

Bellman, R. & Pennington, R. H. 1954 Effects of surface tension and viscosity on Taylor instability. *Q. Appl. Maths* **12**, 151–162.

Chandrasekhar, S. 1961 *Hydrodynamic and Hydromagnetic Stability*. Clarendon.

Daly, B. J. 1967 Numerical study of two fluid Rayleigh–Taylor instability. *Phys. Fluids* **10**, 297–307.

Daly, B. J. 1969 Numerical study of the effect of surface tension on interface instability. *Phys. Fluids* **12**, 1340–1354.

Davis, H. T. 1962 *Introduction to Nonlinear Differential and Integral Equations*. Dover.

Dienes, J. K. 1978 Method of generalized coordinates and an application to Rayleigh–Taylor Instability. *Phys. Fluids* **21**, 736–744.

Emmons, H. W., Chang, C. T. & Watson, B. C. 1960 Taylor instability of finite surface waves. *J. Fluid Mech.* **7**, 177–193.

Fermi, E. & von Neumann, J. 1963 Taylor instability at the boundary of two incompressible liquids. In *Collected Works of John von Neumann*, vol. 6, pp. 431–434. Pergamon.

Harlow, F. H. & Welch, J. E. 1966 Numerical study of large-amplitude free-surface motions. *Phys. Fluids* **9**, 842–851.

Jacobs, J. W. 1986 Three-dimensional Rayleigh–Taylor instability: experiment and theory. Ph.D. dissertation, University of California, Los Angeles.

LAYZER, D. 1955 On the instability of superposed fluids in a gravitational field. *Astrophys. J.* **122**, 1–12.

LEWIS, D. J. 1950 The instability of liquid surfaces when accelerated in a direction perpendicular to their planes. II. *Proc. R. Soc. Lond.* A **202**, 81–96.

MENIKOFF, R. & ZEMACH, C. 1983 Rayleigh–Taylor instability and the use of conformal maps for ideal fluid flow. *J. Comput. Phys.* **51**, 28–64.

MILES, J. W. 1976 Nonlinear surface waves in closed basins. *J. Fluid Mech.* **75**, 419–448.

NAYFEH, A. H. 1969 On the non-linear Lamb–Taylor instability. *J. Fluid Mech.* **38**, 619–631.

PULLIN, D. J. 1982 Numerical studies of surface-tension effects in nonlinear Kelvin–Helmholtz and Rayleigh–Taylor instability. *J. Fluid Mech.* **119**, 507–532.

TAYLOR, G. I. 1950 The instability of liquid surfaces when accelerated in a direction perpendicular to their planes. I. *Proc. R. Soc. Lond.* A **201**, 192–196.

VAN DYKE, M. 1975 *Perturbation Methods in Fluid Mechanics.* Parabolic.

VERMA, G. R. & KELLER, J. B. 1962 Three-dimensional standing waves of finite amplitude. *Phys. Fluids* **5**, 52–56.